Journal of Sound and Vibration 413 (2018) 120–143

Contents lists available at ScienceDirect

Journal of Sound and Vibration

journal homepage: www.elsevier.com/locate/jsvi

Shock isolation performance of a geometric anti-spring isolator

Lixun Yan [a], Shouhu Xuan [b], Xinglong Gong [b,*]

[a] Department of Precision Machinery and Precision Instrumentation, University of Science and Technology of China, Hefei, China
[b] CAS Key Laboratory of Mechanical Behavior and Design of Materials, Department of Modern Mechanics, University of Science and Technology of China, Hefei, China

ARTICLE INFO

Article history:
Received 15 April 2017
Received in revised form 19 September 2017
Accepted 15 October 2017

Keywords:
Shock isolation
Geometric anti-spring isolator
Nonlinear dynamic stiffness

ABSTRACT

In this paper, shock isolation performance of a geometric anti-spring (GAS) isolator is investigated. The static and dynamic stiffness property of GAS isolator is discussed. The mathematical simulation is used to explore the effect of several parameters on shock isolation performance of GAS isolator under a modified half-sine pulse acceleration excitation. Shock isolation experiments of GAS isolator under base acceleration excitation with different excitation amplitudes and payloads are carried out. The results show that the dynamic stiffness characteristic of GAS isolator determines its shock isolation performance. When shock acceleration amplitude is not too large, GAS isolator shows better shock acceleration and absolute displacement isolation performance than the equivalent linear system. The effects of shock acceleration amplitude, payload, and damping on the shock isolation performance of GAS isolator are discussed, which provide guidelines for its further practical application.

1. Introduction

Shock is a common problem existing in many cases, such as rough road excitation in transportation, takeoff and landing of aircraft, earthquake and so on. Usually, it involves a very large force and displacement, which will lead to the damage of sensitive equipment, human discomfort, and other effects. The shock isolation performance of an isolation system is of great importance. Commonly, shock isolation is achieved through energy storage by elastic deformation while shock occurs and energy dissipation to minimize the residual vibration when the shock has finished [1]. The fundamental theory of shock analysis and isolation has been studied in Refs. [2,3], which mostly deals with linear systems.

Nowadays, nonlinear passive isolation systems which can counteract the contradiction between adequate load capacity and low natural frequency of linear systems in low-frequency vibration isolation, have drawn increasing attention [4]. Connecting the negative stiffness mechanism in parallel to the positive stiffness spring is a major method to achieve nonlinear passive isolation systems. Nonlinear isolation system with negative stiffness mechanism, such as horizontally compressed bars [5–7], inclined linear springs [8–11], sliding beams [12], Euler buckled beams [13], cam-roller-spring mechanisms [14]

* Corresponding author. CAS Key Laboratory of Mechanical Behavior and Design of Materials, Department of Modern Mechanics, University of Science and Technology of China, No. 443, Huangshan Road, Shushan District, Hefei 230027, Anhui, China.
E-mail address: gongxl@ustc.edu.cn (X. Gong).

https://doi.org/10.1016/j.jsv.2017.10.024
0022-460X/

Nomenclatures

X_L, Y_L	Horizontal and vertical coordinate of spring's vertex
$\bar{X}_L, \bar{X}_L$	Dimensionless horizontal and vertical coordinate of spring's vertex
G_X, G_Y	Horizontal and vertical load of spring's vertex
$\bar{G}_X, \bar{G}_Y$	Dimensionless horizontal and vertical load of spring's vertex
l, ξ	Actual and dimensionless curve coordinate of differential segment dl
$\theta(l)$	Angle between X-axis positive direction and tangent direction of the segment dl
$Q(l), P(l), M(l)$	Horizontal and vertical internal force, flexural moment of differential segment dl
$w(l), h, L$	Width, thickness, and length of the blade spring
$\overline{F}_y, \overline{y}$	Dimensionless vertical restoring force and vertical displacement of the isolator
m, δ_{st}	Load mass and static deflection of GAS isolator
ω_n	Natural angular frequency of GAS isolator
ω_{st}	Natural frequency calculated by static stiffness of GAS isolator
ω_{el}	Natural frequency of the static stiffness equivalent linear isolator
c, ζ	Viscous damping and damping ratio of the isolator
$B, p(t)$	Acceleration amplitude and pulse shape function of shock excitation

and so on, can realize low or zero net vertical dynamic stiffness without a loss of bearing capacity. At relatively small levels of vibration, the dynamic characteristics of these nonlinear isolation systems [11,15–19] can be captured by the Duffing equation allowing physical insight into the effects of the nonlinearity [20]. Magnetic anti-spring was another method to produce negative stiffness characteristics [21–25]. These negative stiffness structures originated from the permanent magnets and electromagnets were highly effective. However, they were very thermally sensitive and it might induce unwanted couplings to external electromagnetic fields. In addition, using the inherent nonlinear mechanical property or geometric nonlinearity of structures is another exploration to obtain the low dynamic stiffness property. These structures, such as bistable composite plates [26], extreme geometric nonlinear spring [27,28], scissor-like structures [29], shape memory alloy [30] and so on, have great prospects in the practical application of nonlinear low-frequency isolation. However, complex physical mechanisms and nonlinear transcendental equations become a major challenge. Nonetheless, much deep-in research work still needs to be done for their further industrial application.

The aforementioned works mainly were concentrated on the vibration isolation performance of nonlinear isolation systems under harmonic excitation. However, in terms of nonlinear isolation structures, only a little research work has been performed on their shock isolation performance. Snowdon firstly incorporated the nonlinear elements into the theory of shock isolation [31] and found that softening elastic elements could lead to an improved shock isolation. Alexander [32] and Georgiadis et al. [33] considered shock isolation design based on the use of nonlinear energy sinks, which were very easily implementable by means of linear stiffness element.

Ledezma-Ramirez et al. [34] investigated a switchable stiffness isolator for shock isolation, pointed out that the stiffness nonlinearity could be advantageous in improving shock isolation in absolute displacement and acceleration response compared to the linear elastic element. As a negative stiffness element, the buckled beam has also been studied for shock isolation and it exhibited superior performance in linear isolators [35,36]. Tang et al. [37]and Liu et al. [38] investigated the shock isolation response of nonlinear low dynamic stiffness isolator under different types of shock inputs and found that a nonlinear isolator could outperform the linear one if shock excitation amplitude is small.

The geometrical anti-spring (GAS) structure was proposed by Cella [39] for the purpose of seismic attenuation and it was successfully applied in optical table prototype designed for advanced LIGO (Laser Interferometer Gravitational-wave Observatory) [40] and external injection bench of the advanced Virgo gravitational wave detector [41]. In contrast to the nonlinear isolator, the advantages of GAS isolator include structurally simple and compactness, space saving and insensitive to temperatures or external electromagnetic fields, and so on. However, except for the seismic attenuation in gravitational wave observatory, GAS isolator has not been applied in any other vibration reduction application. And the thorough shock isolation performance of this nonlinear isolation structure, which is of great importance for its further practical application, has not been discussed.

In this paper, a geometric anti-spring isolator is developed and its shock isolation performance is theoretically and experimentally studied. The nonlinear stiffness and natural frequency characteristics of the GAS isolator are theoretically investigated using a micro-element method in Section 2. In Section 3, shock isolation performance of this nonlinear isolator under the excitation of the modified half-sine pulse is explored through mathematical simulation. The effects of the geometric parameter, excitation amplitude, payload, and damping on shock isolation performance of GAS isolator are considered. In Section 4, shock isolation experiments of GAS isolator under base acceleration excitation with different excitation amplitudes and payloads are performed by an electromagnetic vibration table, which validates the simulation results. Some conclusions are given in Section 5.

2. Geometric anti-spring isolator

GAS isolator (Fig. 1(a) and (b)) consists of several quasi-trapezoidal blade springs (Fig. 1(c)). The blade springs are built flat and bent under the load. Their bottoms are radially clamped to a base structure and vertices are connected together. The external forces including vertical load and horizontal constraint force are applied to the vertex. The width of blade spring is represented by w(l), with $l \in [0, \ L]$. The shape function of blade spring is

$$\gamma(\xi) = \frac{w(l)}{w(0)} = [c_1 + c_2\cos(\beta\xi) + c_3\sin(\beta\xi)]^{-1} \tag{1}$$

Where $\xi = l/L$, $c_1 = -0.377$, $c_2 = 1.377$, $c_3 = 0.195$ and $\beta = 1.361$. The width w(l) and length L of blade spring are much larger than constant thickness h.

2.1. Theoretical analysis

Due to the radial symmetricity, the mechanical property of GAS isolator can be characterized with a single blade spring (Fig. 1(d) and (e)). The effects of shear deformation and extensibility in the longitudinal direction are all neglected. X_L and Y_L represent the horizontal and vertical coordinate of blade springs' vertex. G_X and G_Y denote the horizontal constraint load and vertical load. P(l), Q(l) and M(l) are the horizontal internal force, vertical internal force and bending moment of differential segment dl, respectively. $\theta(l)$ is the angle between the positive X-axis direction and tangent direction of dl. The relationship between variables X, Y and θ can be written as

$$\frac{dX}{dl} = \cos\theta, \quad \frac{dY}{dl} = \sin\theta \tag{2}$$

The relationship between the curvature and bending moment can be written as

$$\frac{1}{\rho} = -\frac{d\theta}{dl} = \frac{M}{EI} \tag{3}$$

where EI denotes the flexural rigidity of blade spring and $I(l) = d^3w(l)/12$.

According to static force equilibrium, two following equations can be obtained

$$\frac{dP}{dl} = 0, \quad \frac{dQ}{dl} = 0 \tag{4}$$

Here, the gravity of dl is neglected because the whole mass of blade springs is very small compared with base structures and payload mass. Therefore, internal forces of dl keep constant and $P = G_X, Q = G_Y$.

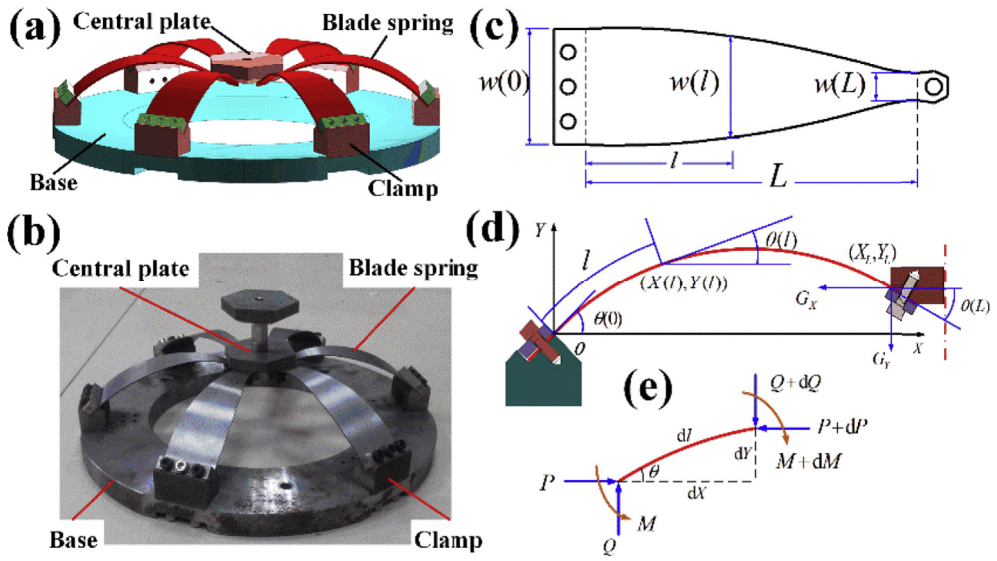

Fig. 1. The model of the GAS isolator. (a) Schematic diagram of the GAS isolator. (b) Photograph of the GAS isolator. (c) The shape of blade spring. (d) A simplified model of the GAS isolator. (e) A differential segment of the simplified model.

Likewise, bending moment equilibrium of dl can be written as

$$\mathrm{M}+\mathrm{P}\frac{\mathrm{d}Y}{2}+(P+\mathrm{d}P)\frac{\mathrm{d}Y}{2}=M+\mathrm{d}M+Q\frac{\mathrm{d}X}{2}+(Q+\mathrm{d}Q)\frac{\mathrm{d}X}{2} \tag{5}$$

Substituting Eqs. (2) and (4) into Eq. (5) produce a simplified equation

$$\frac{\mathrm{d}M}{\mathrm{d}l}=P\sin\theta-Q\cos\theta \tag{6}$$

Introducing a dimensionless transformation

$$\begin{aligned}&\tilde{X}=\frac{X}{L}=\int_0^{\xi}\cos(\xi)\mathrm{d}\xi,\ \ \tilde{Y}=\frac{Y}{L}=\int_0^{\xi}\sin(\xi)\mathrm{d}\xi,\\&\tilde{G}_X=\frac{L^2G_X}{EI(0)},\ \ \tilde{G}_Y=\frac{L^2G_Y}{EI(0)},\ \ \tilde{M}=\frac{LM}{EI(0)}\end{aligned} \tag{7}$$

then, the static mechanical equation of GAS structure can be given as

$$\begin{aligned}&\frac{\mathrm{d}\theta(\xi)}{\mathrm{d}\xi}=\gamma(\xi)\tilde{M},\ \ \frac{\mathrm{d}\tilde{M}}{\mathrm{d}\xi}=\tilde{G}_X\sin\theta(\xi)-\tilde{G}_Y\cos\theta(\xi)\\&\theta(0)=\pi/4,\ \ \theta(1)=-\pi/6\end{aligned} \tag{8}$$

2.2. Characteristics of stiffness and natural frequency

In general, an exact analytical solution of Eq. (8) cannot be obtained theoretically with an explicit expression formulation. Using a MATLAB (Matlab 2016a) program, the approximate numerical solution of Eq. (8) is achieved. The relationship between dimensionless vertical force $\overline{F}_y$ and vertical displacement $\overline{y}$ is obtained further, where $\overline{F}_y=-\tilde{G}_Y$ is restoring force and $\overline{y}=\tilde{Y}_L\big|_{\tilde{G}_Y=0}-\tilde{Y}_L$ is the static vertical displacement of GAS isolator when subjected to a vertical payload $\tilde{G}_Y$.

Fig. 2(a) shows the dimensionless force-displacement ($\overline{F}_y$–$\overline{y}$) curve. Typically, the numerical results are given with different shapes of scattering dots while the polynomial fitting results are given with different types of lines.

The dimensionless horizontal coordinate $\tilde{X}_L$ of blades spring's vertex is the key parameter to decide the mechanical nonlinearity of GAS isolator and is referred to geometric parameter for the sake of convenience. The relationship between dimensionless restoring force and vertical displacement for different geometric parameters can be accurately fitted by a seven order polynomial function

$$\overline{F}_y(\overline{y})=a_1\overline{y}+a_2\overline{y}^2+a_3\overline{y}^3+a_4\overline{y}^4+a_5\overline{y}^5+a_6\overline{y}^6+a_7\overline{y}^7 \tag{9}$$

The fitting coefficients are denoted by $a_i(i=1,2,3,4,5,6,7)$ (Table 1).

In order to describe the nonlinearity stiffness characteristic of GAS isolator more conveniently, the concepts of static stiffness, dynamic stiffness and dynamic *vs* static stiffness ratio are discussed. Static stiffness is equal to the ratio of vertical payload to vertical deflection. Dynamic stiffness is defined as the first order derivative to restoring force with respect to displacement. The dynamic vs static stiffness ratio describes the relative size of bearing capacity and low-frequency isolation capacity of nonlinear isolators. Theoretically, the smaller the dynamic vs static stiffness ratio is, the better the low-frequency isolation performance of the nonlinear isolator will be.

Fig. 2(b) and (c) show the dimensionless stiffness characteristic of the GAS isolator. It can be seen that, with the increase of geometric parameter, the minimum dynamic stiffness of GAS isolator increases and static displacement at the minimum dynamic stiffness point decreases. However, the rated load at the minimum stiffness point almost does not change as geometric parameter increases.

The curves of static stiffness, dynamic stiffness, and dynamic vs static stiffness ratio of the GAS isolator at the minimum dynamic stiffness point are shown in Fig. 2(d). It can be seen that dynamic vs static stiffness ratio of the GAS isolator at the minimum dynamic stiffness point decreases with the decrease of the geometric parameter. With enough bearing capacity, the GAS isolator can realize very low dynamic stiffness when the geometric parameter is settled as small as possible.

According to the linear vibration theory, natural frequency of GAS isolator under a payload G_Y can be calculated by

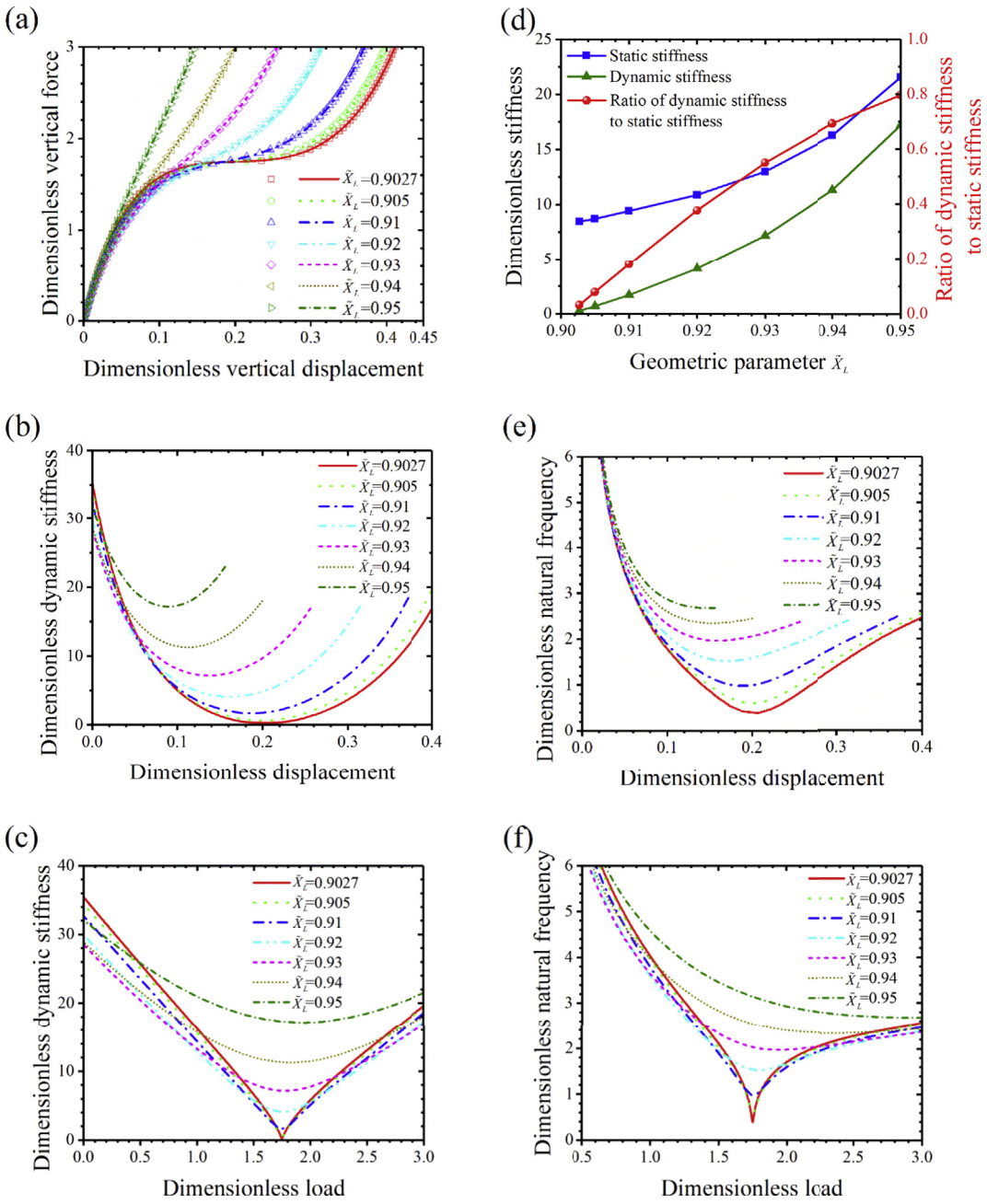

Fig. 2. (a) Curve of dimensionless force vs dimensionless displacement of the GAS isolator. (b) Dimensionless dynamic stiffness vs dimensionless displacement. (c) Curve of dimensionless dynamic stiffness vs dimensionless payload. (d) Static stiffness, dynamic stiffness and dynamic vs static stiffness ratio of the GAS isolator at the minimal dynamic stiffness working point. (e) Curve of dimensionless natural frequency vs dimensionless displacement. (f) Curve of dimensionless natural frequency vs dimensionless payload.

$$\omega_n^2 = \frac{g}{G_Y}\frac{\partial F_y}{\partial y} = \frac{g}{L}\frac{1}{\tilde{G}_Y}\frac{\partial \overline{F}_y}{\partial \overline{y}}$$

Here, $\overline{F}_y = \frac{L^2 F_y}{EI(0)}$. The dimensionless natural frequency of GAS isolator can be written as follow

$$\tilde{\omega}_n^2 = \frac{L}{g}\omega_n^2 = \frac{1}{\tilde{G}_Y}\left(\frac{\partial \overline{F}_y}{\partial \overline{y}}\right)$$

Table 1
Polynomial fitting coefficients of force vs displacement curve.

$\bar{X}_L$	a_1	a_2	a_3	a_4	a_5	a_6	a_7
0.9027	35.20	−329.85	1991.34	−8291.93	22022.09	−32194.61	19948.43
0.905	34.33	−318.76	1912.45	−7915.64	21021.68	−30829.86	19258.79
0.91	32.63	−298.54	1808.39	−7651.96	21186.12	−32719.64	21726.28
0.92	29.91	−264.02	1660.20	−7494.34	23193.40	−40935.25	31675.37
0.93	28.50	−240.06	1632.69	−8239.71	30027.20	−63475.03	59488.88
0.94	28.86	−222.00	1593.47	−8398.50	34082.22	−82434.32	91965.84
0.95	32.09	−219.61	1689.49	−8845.06	37265.10	−92945.24	114202.6

Fig. 2(e) and (f) show curves of the dimensionless natural frequency of GAS isolator with different geometric parameters. It can be seen that the natural frequency of GAS isolator decreases with increasing of the payload when $\bar{X}_L > 0.93$. However, when $\bar{X}_L \leq 0.93$, the minimum natural frequency approximately keeps at the same payload.

3. Mathematical simulation and result discussion

3.1. Dynamic mechanical model

To investigate shock isolation performance of GAS isolator, a Matlab/Simulink program based on four order Runge-Kutta algorithm is established to simulate shock isolation response of GAS isolator. A single degree of freedom viscously damped nonlinear vibration isolation system simplified from GAS isolator is shown in Fig. 3(a).

According to previous theoretical analysis results, the relationship between actual restoring force F_y and vertical displacement y of GAS isolator can be written as follow

$$F_y(y) = \frac{EI(0)}{L^2}\sum_{i=1}^{7} a_i\left(\frac{y}{L}\right)^i \tag{10}$$

When subjected to a base excitation, governing equation of motion of GAS isolator with a viscous damping c can be given by

$$\mathrm{m}\frac{\mathrm{d}^2 z}{\mathrm{d}t^2} + \mathrm{c}\frac{\mathrm{d}z}{\mathrm{d}t} + r(z) = -m\frac{\mathrm{d}^2 v}{\mathrm{d}t^2} \tag{11}$$

where $z = u - v$ represents the relative displacement between base and load mass. $r(z) = F(\delta_{st}) - F(\delta_{st} - z)$ donates restoring force of the single degree of freedom system at the static equilibrium position. δ_{st} is static deformation of GAS isolator under payload G_y.

Introducing the dimensionless parameters

$$\hat{z} = \frac{z}{\delta_{st}},\ \omega_{st}^2 = \frac{g}{\delta_{st}},\ \hat{t} = t\omega_{st},\ \zeta = \frac{c}{2m\omega_n},\ s = \frac{\omega_n}{\omega_{st}},$$

$$\frac{\mathrm{d}^2 v}{\mathrm{d}t^2} = Bp(t),\ \hat{B} = \frac{B}{g},\ \hat{r}(\hat{z}) = 1 - \frac{F[\delta_{st}(1-\hat{z})}{F(\delta_{st})},$$

Eq. (11) can be written as

$$\frac{\mathrm{d}^2\hat{z}}{\mathrm{d}\hat{t}^2} + 2s\zeta\frac{\mathrm{d}\hat{z}}{\mathrm{d}\hat{t}} + \hat{r}(\hat{z}) = -\hat{B}p\left(\frac{\hat{t}}{\omega_{st}}\right) \tag{12}$$

where B is shock maximum acceleration amplitude and $p(t)$ is shape function of half sine pulse.

Actual half-sine acceleration shock signal generated by vibration table is shown in Fig. 3(b) and (c). In order to simulate this shock excitation signal, two compensation signals are added to the main pulse of the theoretical half-sine signal. The amplitude ratio κ of compensation signals to main pulse signal is set as 0.2 in this work.

Fig. 3(d) shows the shape of modified half sine pulse of a unity acceleration amplitude with different durations. The shape function of modified half-sine pulse is as follows

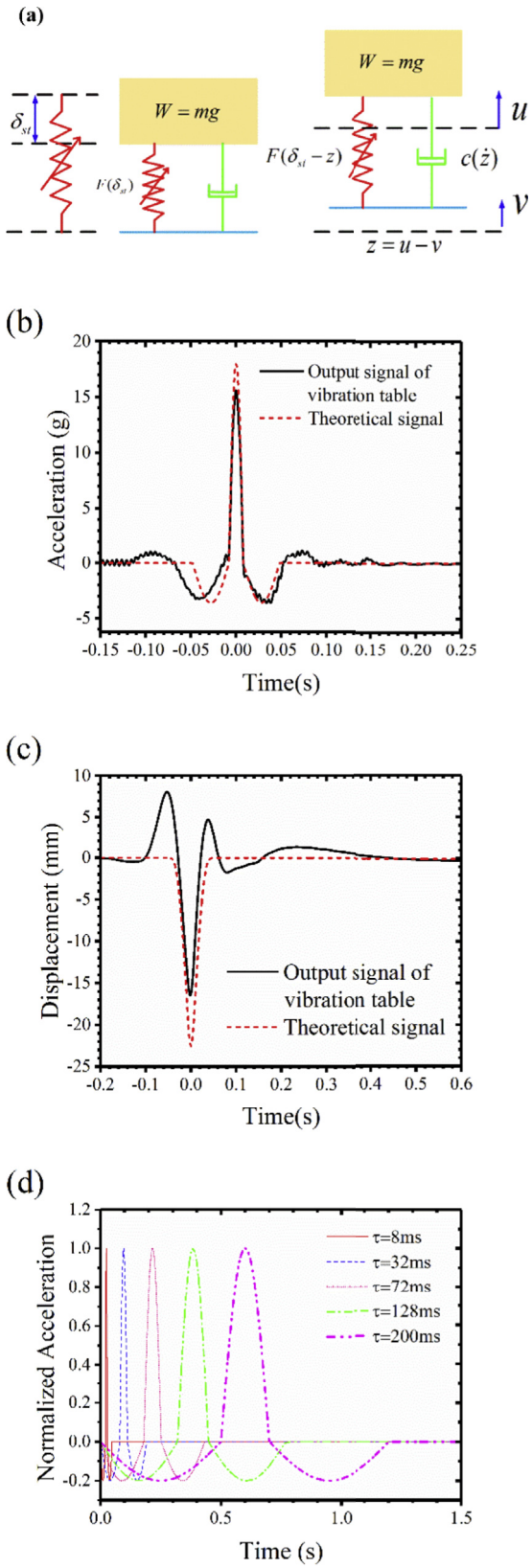

Fig. 3. Dynamic mechanical model of GAS isolator under base shock excitation. (a) Single degree of freedom viscously damped nonlinear vibration isolation system under base excitation. (b) Half-sine acceleration shock signal generated by vibration table and theoretical simulation signal. (c) Excitation displacement signals of vibration table and theoretical simulation signal. (d) Shape of the modified half-sine pulse with different durations.

$$p\left(\frac{\hat{t}}{\omega_{st}}\right)=\begin{cases}-\kappa\sin\dfrac{\pi}{\tau_1}\dfrac{\hat{t}}{\omega_{st}}, & 0\le\dfrac{\hat{t}}{\omega_{st}}\le\tau_1\\ -\sin\dfrac{\pi}{\tau}\left(\dfrac{\hat{t}}{\omega_{st}}-\tau_1\right), & \tau_1\le\dfrac{\hat{t}}{\omega_{st}}\le\tau_1+\tau\\ -\kappa\sin\dfrac{\pi}{\tau}\left(\dfrac{\hat{t}}{\omega_{st}}-\tau_1-\tau\right), & \tau_1+\tau\le\dfrac{\hat{t}}{\omega_{st}}\le2\tau_1+\tau\end{cases}\tag{13}$$

where τ is the duration of main pulse and $\tau_1=\tau/2\kappa$.

3.2. Method of evaluating shock isolation performance

To evaluate shock isolation performance of nonlinear vibration isolation system, shock acceleration ratio (SAR), shock displacement ratio (SDR) and relative displacement ratio (RDR), which are related to the forces transmitted through the isolator and available deformation space or clearance, are used [34,37].

$$\mathrm{SAR}=\frac{|\ddot{u}|_{max}}{|\ddot{v}|_{max}}\tag{14}$$

$$\mathrm{SDR}=\frac{|u|_{max}}{|v|_{max}}\tag{15}$$

$$\mathrm{RDR}=\frac{|u-v|_{max}}{|v|_{max}}\tag{16}$$

The force transmitted through elastic and damping elements from base excitation is equal to the product of mass and acceleration. If SAR is large, forces transmitted through the elastic and damping elements are considerable. SDR gives the maximum displacement transmissibility. A large SDR means vibration isolation performance of nonlinear isolator is poor. RDR shows the size of relative deformation of the nonlinear isolator, and a large RDR means a large deflection.

These three indexes are normally presented graphically as a function of severity parameter β. For a linear system, severity parameter is defined as

$$\beta=\frac{T}{2\tau}\tag{17}$$

where T is the natural period of the linear system and τ is the duration of shock main pulse. According to the size of β, shock transmissibility can be divided into three regions. When $\beta\gg1$, shock duration is small compared to natural period of isolation system and shock signal is isolated, which is called shock isolation region. When $\beta\ll1$, shock duration is too long compared to natural period of isolation system and shock excitation is similar to a slow static loading, which is equivalent static region. When β is close to 1, response amplitude of isolators is larger than excitation amplitude, which is shock amplification region.

Because the natural period of nonlinear isolator varies with vibration levels, which depend on both excitation amplitude and duration of the pulse, severity parameter β is redefined as the ratio of the natural period of the equivalent linear system of GAS isolator to duration of shock main pulse. Therefore, severity parameter is given as follows

$$\begin{aligned}\beta&=\frac{\pi}{\tau\omega_{el}}\\ \omega_{el}&=\sqrt{\frac{g}{L\hat{\delta}_{kmin}}}\end{aligned}\tag{18}$$

Here, $\hat{\delta}_{kmin}$ is dimensionless static deformation of GAS isolator working at the minimal dynamic stiffness point.

3.3. Simulation results and discussion

In this section, the effects of the geometric parameter, excitation amplitude, static payload and viscous damping ratio on the shock isolation performance of GAS isolator are discussed. Three shock isolation performance indexes are plotted with the severity parameter ranging from 0.1 to 100.

3.3.1. Effect of the geometric parameter

Fig. 4 shows shock time domain response of GAS isolator with a shock main pulse duration of 11 ms. GAS isolator works at the minimum dynamic stiffness point with the same damping ratio of 0.1 and shock excitation acceleration amplitude is 30 g.

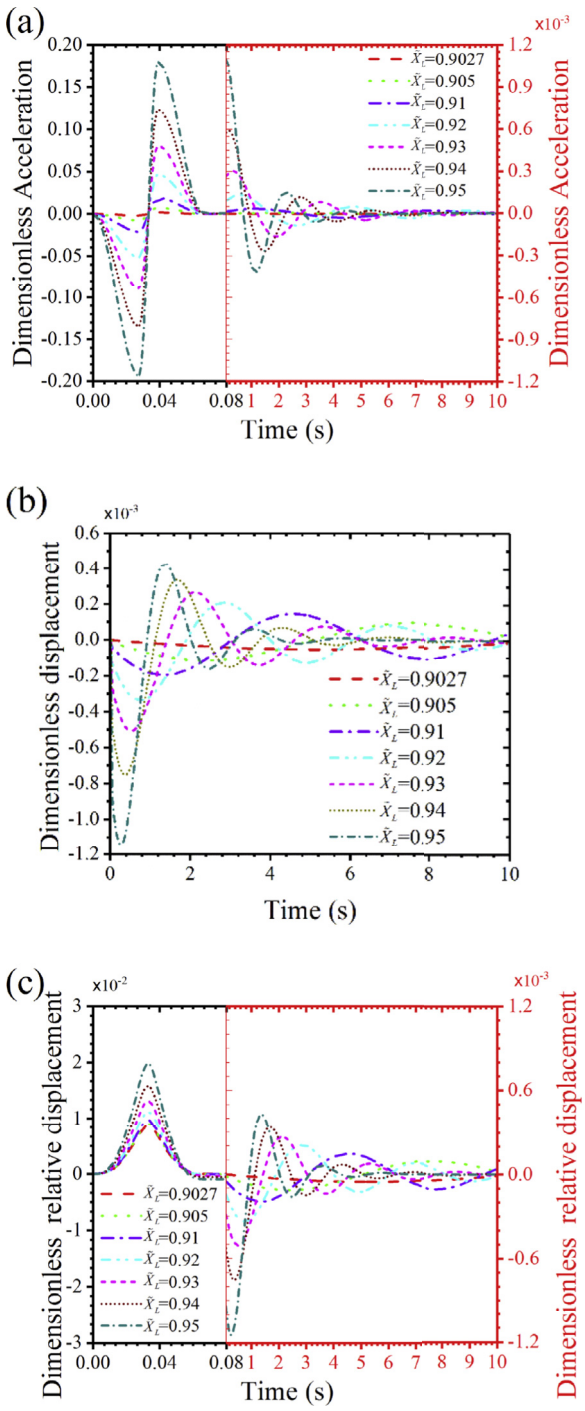

Fig. 4. Shock time domain response of GAS isolator with different geometric parameters. (a) shows the time-history diagram of responsive acceleration signals. (b) is for responsive displacement signals. (c) is for relative displacement signals.

The response acceleration and relative displacement of the GAS isolator in the shock duration are large. However, when shock excitation finishes, these two kinds of response signal decrease sharply. As the geometric parameter increases, shock response maximum peak increases and natural period of residual vibration decreases. This is explained by the fact that the effective dynamic stiffness of GAS isolator increases as geometric parameter increases.

The shock transmissibility of GAS isolator with different geometric parameters is shown in Fig. 5. It can be concluded that when severity parameter is large, i.e. in shock isolation region, with the increase of geometric parameter, SAR and SDR

increase but RDR decreases. SAR and SDR of GAS isolator are lower than that of the equivalent linear isolator when the geometric parameter is small. Better shock isolation performance in terms of responsive acceleration and displacement will be obtained if the geometric parameter is adjusted as small as possible. However, RDR of GAS isolator is larger than that of equivalent linear isolator except for that geometric parameter is larger than 0.93.

When the geometric parameter is small, the effective dynamic stiffness of GAS isolator is much smaller than static stiffness. So GAS isolator shows better shock isolation performance compared to the equivalent linear isolator. When the geometric parameter is large, the effective dynamic stiffness increases to be larger than static stiffness, which will lead to a deterioration effect on the shock isolation performance of GAS isolator. The range of amplification region and transmissibility curve peak of the GAS isolator are larger than that of the equivalent linear isolator.

In amplification region, vibration displacement amplitude of the isolator increases and the effective dynamic stiffness of GAS isolator increases quickly, which leads the abrupt increase of the shock transmissibility. When severity parameter is small, i.e. in equivalent static loading region, shock excitation is similar to a static loading. So SAR and SDR tend to 1, and RDR approaches to 0.

3.3.2. Effect of shock acceleration amplitude

To study the effect of shock acceleration amplitude on the shock isolation performance, geometric parameter, dimensionless payload, and viscous damping ratio are set as 0.92, 1.75 and 0.1, respectively.

Fig. 6 shows shock time domain response of GAS isolator under different shock excitation amplitudes with a shock pulse duration of 11 ms. As the shock acceleration amplitude increases, response amplitude of GAS isolator increases. Differently, natural period of residual vibration almost keeps the same under different excitation amplitudes. This is because that shock duration is small compared to the natural period of the GAS isolator and shock excitation is isolated. The effective dynamic stiffness of GAS isolator shows little change with the increase of shock amplitudes.

Fig. 7 shows the shock transmissibility of GAS isolator under different shock acceleration amplitudes. It can be seen that increasing excitation amplitude does not influence shock transmissibility in shock isolation region and in equivalent static loading region. However, when severity parameter varies from 1 to 20, with the increase of shock acceleration amplitude, shock transmissibility curve shows a rightward movement. In addition, the peak of transmissibility curve increases as shock amplitude increases. When shock amplitude is small, SAR and SDR of GAS isolator are less than that of the equivalent linear isolator in shock isolation region.

With the increase of vibration amplitude, the effective dynamic stiffness of GAS isolator increases and its natural period decreases. Therefore, as shock excitation acceleration amplitude increases, the shock excitation level enters the shock amplification region more and more early.

3.3.3. Effect of payload

To study the effect of payloads on the shock isolation performance of GAS isolator, geometric parameter, shock acceleration amplitude and damping ratio are set as 0.92, 30 g and 0.1, respectively. The dimensionless payload ranges from 1.47 to 2.10, and the dimensionless rated load is 1.75.

Fig. 8 shows shock time domain response of GAS isolator under different payloads with a shock pulse duration of 11 ms. It can be seen that as payload increases from 1.47 to 1.75, shock response magnitude of GAS isolator decreases rapidly. However, when payload is larger than the rated load (1.75), with the increase of payload, response acceleration peak increases and response displacement peak shows a slow decrease. Meantime, natural period of residual vibration firstly increases and then decreases. This is resulted from that the effective dynamic stiffness of GAS isolator first decreases and then increases as payload increases.

Fig. 9 shows shock transmissibility of GAS isolator under different payloads. In shock isolation region, SAR and SDR first decrease and then increase as payload increases. The minimal shock acceleration ratio is obtained when payload is equal to the rated load. If the payload is not far away from the rated load, shock transmissibility of GAS isolator will be still smaller than that of the equivalent linear isolator. This agrees with the dynamic stiffness characteristic of the GAS isolator with different loads. When the payload is equal to the rated load, natural period of the GAS isolator is larger than that with other payloads and shock isolation performance is better.

3.3.4. Effect of linear viscous damping

In order to study the effect of linear viscous damping on the shock isolation performance of GAS isolator, geometric parameter, dimensionless payload and shock acceleration amplitude are set as 0.92, 1.75 and 30 g.

Fig. 10 shows time domain response of GAS isolator with different viscous damping ratios. As damping ratio increases, response acceleration peak of GAS isolator increases in shock duration time but the residual vibration is attenuated fast. When damping ratio is larger, the maximum displacement response appears earlier. The peak of relative displacement almost does not change as damping ratio increases in shock duration time.

Fig. 11 shows shock transmissibility curve of the GAS isolator with different linear damping ratios. It can be seen that viscous damping has a similar influence on shock isolation performance of both nonlinear and linear isolators. As damping

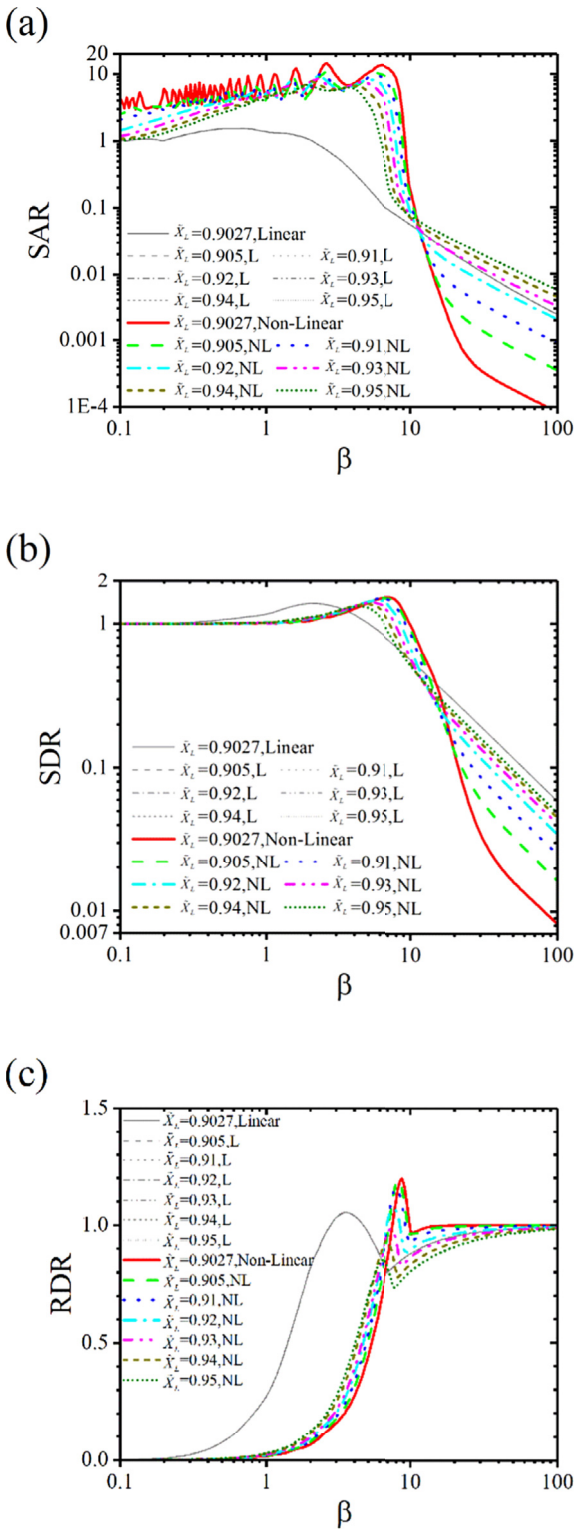

Fig. 5. Shock transmissibility of GAS isolator with different geometric parameters. (a) Shock acceleration ratio (SAR). (b) Shock displacement ratio (SDR). (c) Relative displacement ratio (RDR). L represents equivalent linear isolator and NL is for GAS isolator.

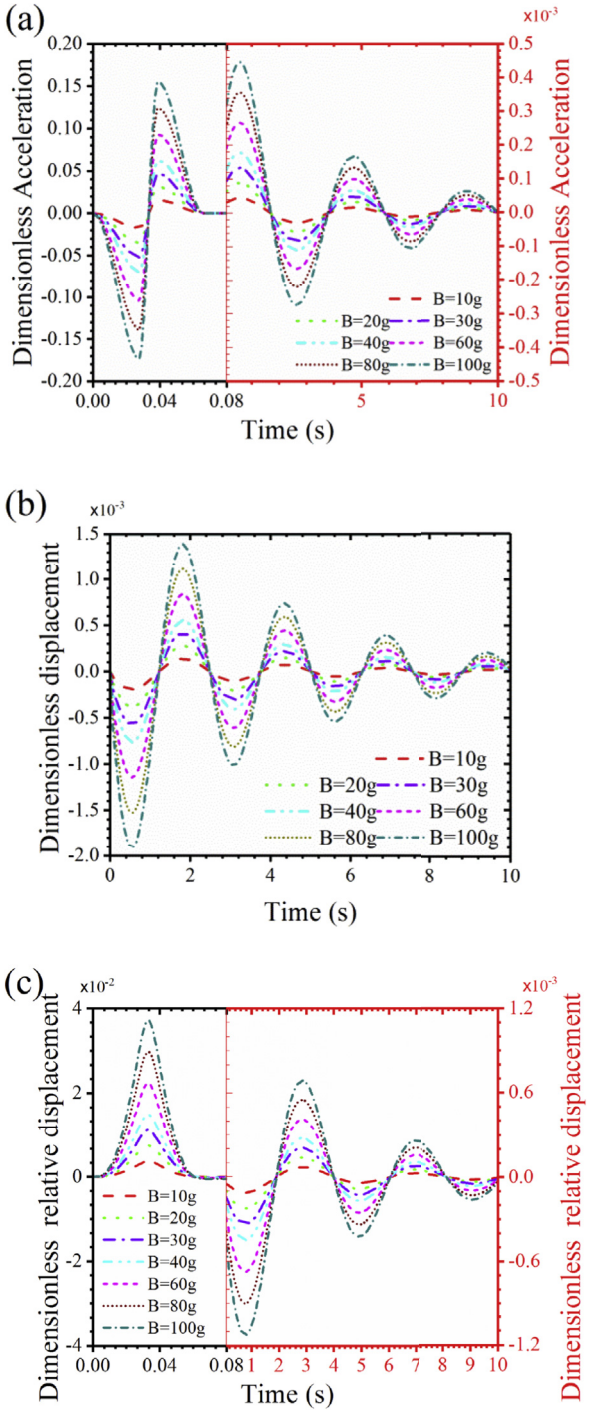

Fig. 6. Time domain shock response of GAS isolator under different excitation amplitudes. (a) shows the time-history diagram of responsive acceleration signals. (b) is for responsive displacement signals. (c) is for relative displacement signals.

ratio increases, transmissibility curve peak diminishes apparently in shock amplification region. However, in shock isolation region, as damping ratio increases, SAR increases gradually, SDR decreases first and then increases, and RDR decreases gradually. When the damping ratio is 0.2, SDR is the smallest in shock isolation region.

In shock amplification region, the amount of energy dissipation increases as damping increases. Therefore, shock transmissibility decreases with increasing of the damping. In shock isolation region, both deflection and elastic restoring force of GAS isolator are very small. When the damping ratio is small, the damping force is also weak during shock duration

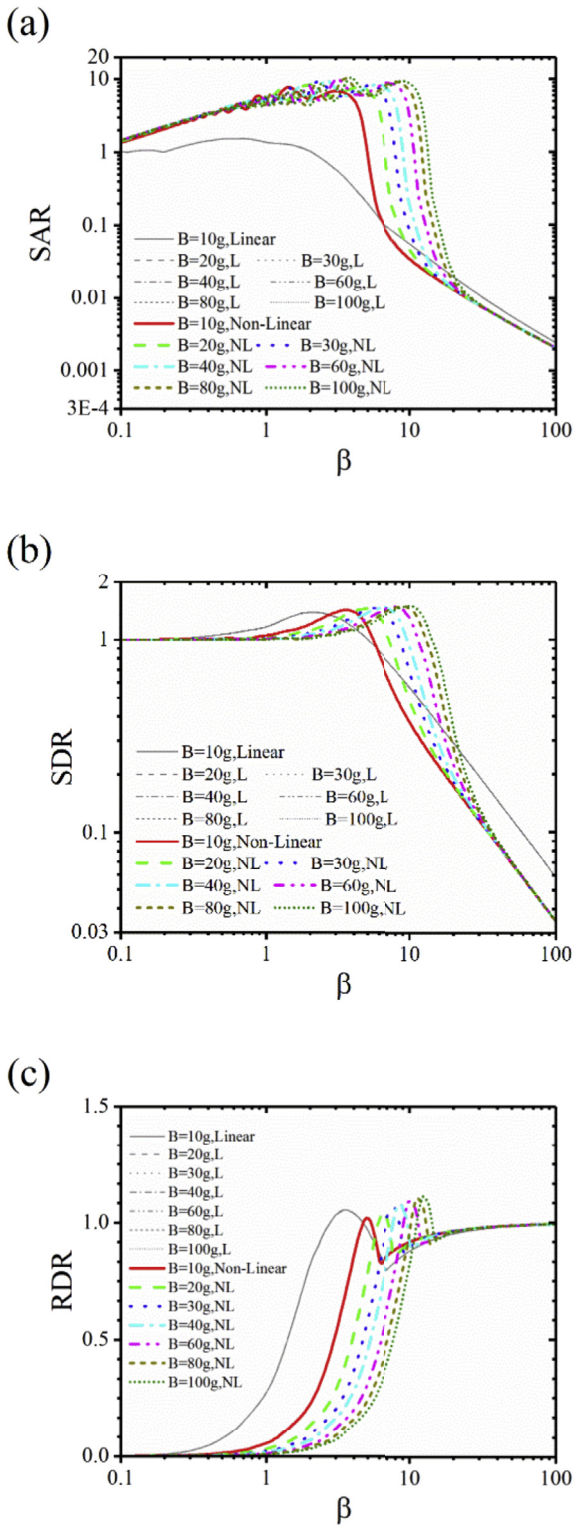

Fig. 7. Shock transmissibility of GAS isolator for different shock excitation amplitudes. (a) Shock acceleration ratio (SAR). (b) Shock displacement ratio (SDR). (c) Relative displacement ratio (RDR). L represents equivalent linear isolator and NL is for GAS isolator.

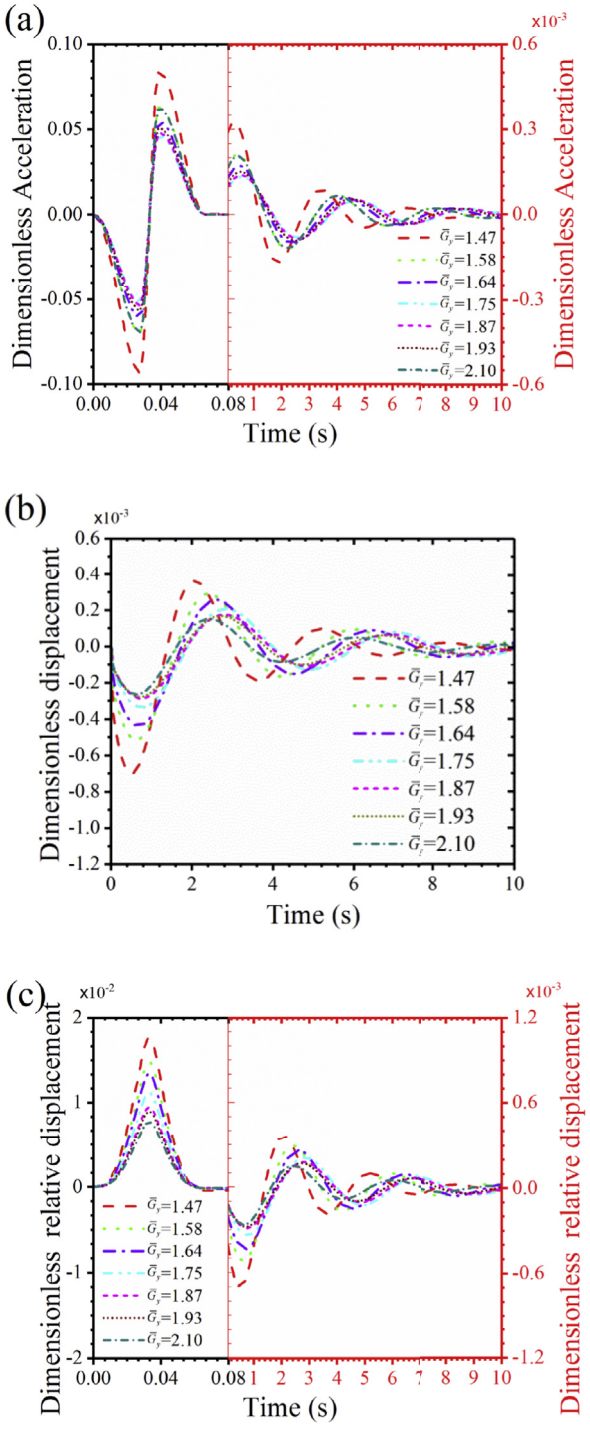

Fig. 8. Time domain shock response of GAS isolator under different payloads. (a) shows the time-history diagram of responsive acceleration signals. (b) is for responsive displacement signals. (c) is for relative displacement signals.

time, so force transmissibility of GAS isolator is small. However, energy dissipation capacity is weak when damping is small, so deformation of GAS isolator will be large. As damping increases, damping force increases. Therefore, force transmissibility of GAS isolator increases. According to the energy conversation law, relative displacement of GAS isolator decreases as force increases.

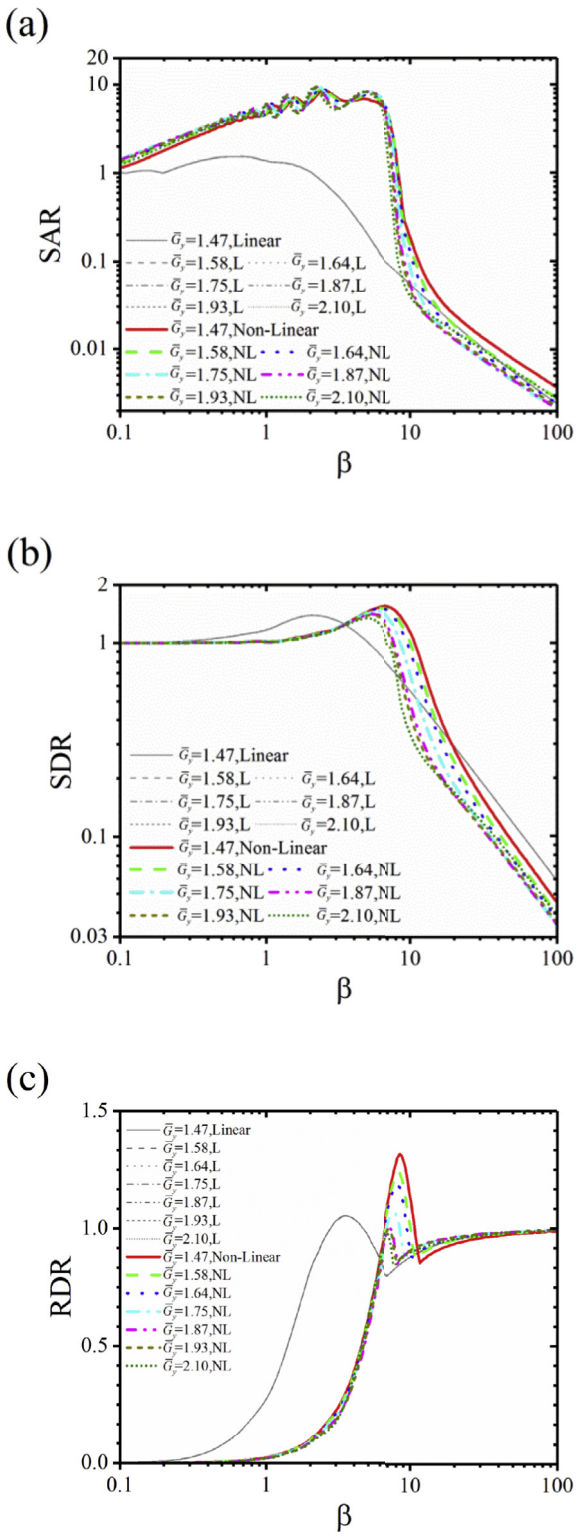

Fig. 9. Shock transmissibility of GAS isolator for different payloads. (a) Shock acceleration ratio (SAR). (b) Shock displacement ratio (SDR). (c) Relative displacement ratio (RDR). L represents equivalent linear isolator and NL is for GAS isolator.

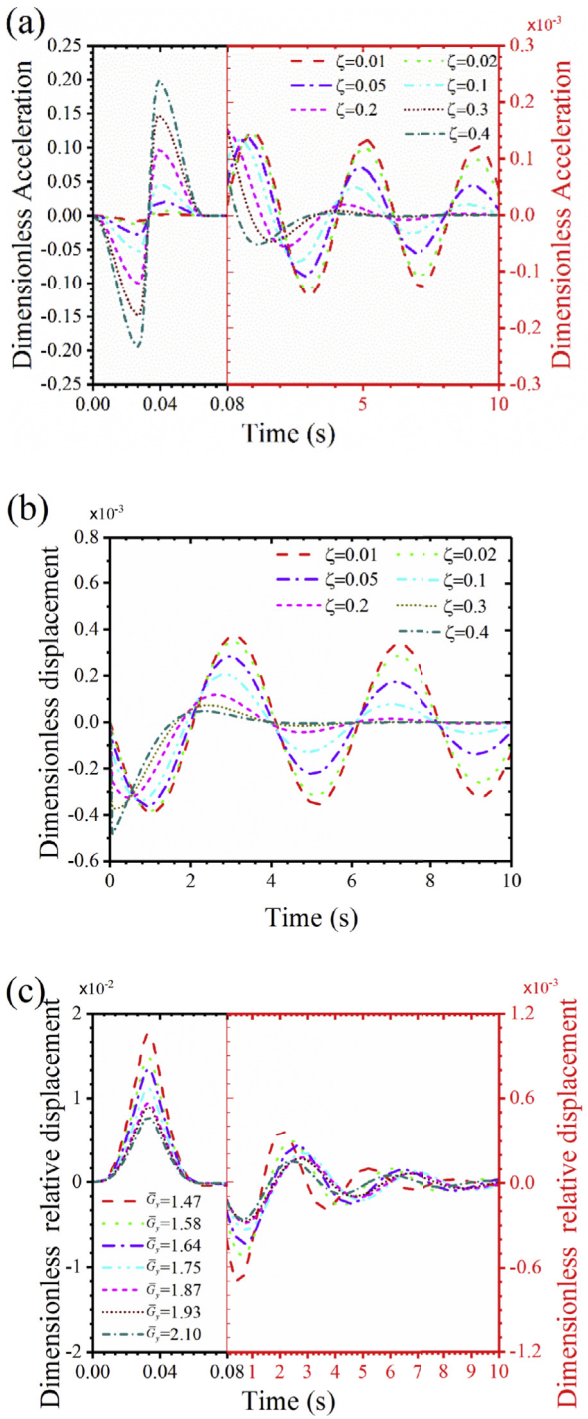

Fig. 10. Time domain shock response of GAS isolator with different viscous damping ratios. (a) shows the time-history diagram of responsive acceleration signals. (b) is for responsive displacement signals. (c) is for relative displacement signals.

4. Shock experiment and result discussion

4.1. Experiment setup

To experimentally investigate shock isolation performance of GAS isolator, a geometric anti-spring isolator with a geometric parameter of 0.92 is fabricated and a single degree of freedom experimental system (Fig. 12) is developed. The actual

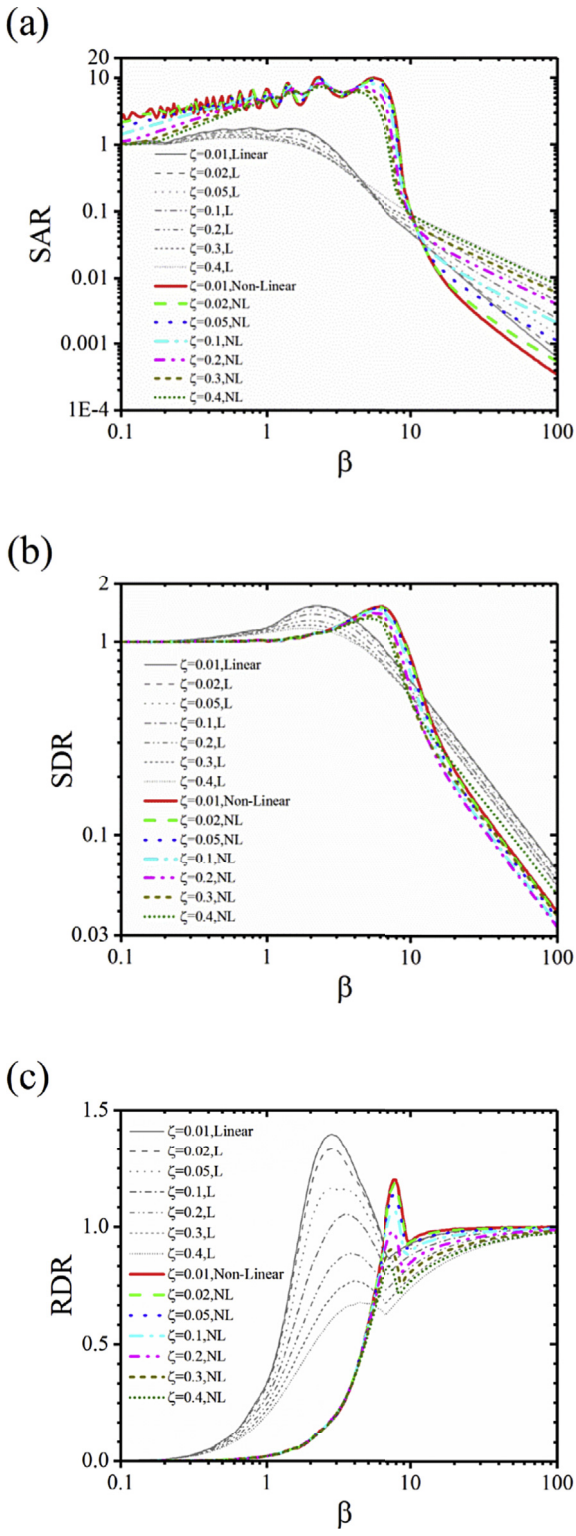

Fig. 11. Shock transmissibility of GAS isolator with different linear viscous damping ratios. (a) Shock acceleration ratio (SAR). (b) Shock displacement ratio (SDR). (c) Relative displacement ratio (RDR). L represents equivalent linear isolator and NL is for GAS isolator.

Table 2
Actual design parameters for GAS isolator.

Parameters	Values
Base width $w(0)$	36 mm
Effective length L	120 mm
Thickness d	0.78 mm
Yield strength σ_s	1665 MPa
Young's modulus E	196 GPa

design parameters of the GAS isolator are given in Table 2. The design load of each blade is 34 N, and the rated load of GAS isolator consisting of six blade springs is 204 N. The photograph of the GAS isolator is shown in Fig. 1(b), with diameter 318 mm, high 90 mm, and total weight 8 kg.

The single degree of freedom experimental system (Fig. 12) is made up of three parts: a primary vibration isolation system, a base excitation system, and a data acquisition system. The primary vibration isolation system consists of installation base, GAS isolator, and load mass. The load mass is composed of a big cylinder (15.9 kg) and several small mass blocks (2.5 kg). The GAS isolator is installed between the base and load mass. Four linear guides are fixed to the installation base to keep vertically translational motion of load mass.

The excitation system is composed of a signal generator, a power amplifier, and an electro-dynamic vibration table (DC-4000-40/SC-0808). The maximum working load, output displacement, output acceleration, and work frequency range are 500 kg, 76 mm, 100 g (1 g = 9.8 ms^{-2}) and 1–2000 Hz, respectively.

The data acquisition system includes four piezoelectric charge-type accelerometers, four charge amplifiers, a dynamic data analyzer (Signal Calc ACE) and personal computers (PC). The shock responsive acceleration signals of the GAS isolator are collected with four accelerometers. Two of them are connected to charge amplifiers with twice integral function and the displacement signals of the base and mass can be acquired. Dynamic data analyzer and PC are used to analyze response signals to obtain the evaluation result of shock isolation performance. To make the time history signals much clear, a bandpass filter with cutoff frequencies of 0.5 Hz and 150 Hz is used for the post-processing.

4.2. Experiment results and discussion

To experimentally investigate the shock isolation performance of GAS isolator under different excitation levels, load mass is chosen as 20.9 kg. Duration of shock pulse ranges from 12 ms to 16 ms with an interval of 1 ms and shock acceleration amplitudes are 6 g, 9 g, 12 g, 15 g, and 18 g. For the case of different payloads, shock acceleration amplitude is 8 g. Load mass ranges from 15.9 kg to 23.4 kg with an interval of 2.5 kg and duration of shock pulse is from 12 ms to 22 ms with an interval of 2 ms.

4.2.1. Time domain results

Fig. 13 shows shock time domain response of GAS isolator with a payload of 20.9 kg under a shock excitation of 18 g and 16 ms. The maximum response acceleration and relative displacement occur during shock duration time but the maximum response displacement appears when shock finishes. The acceleration frequency spectrum of GAS isolator includes extra signals near 15 Hz and 23 Hz, which may be caused by defects of linear guides.

Shock time domain response of GAS isolator under different excitation amplitudes and different payloads are shown in Fig. 14. Acceleration signal is presented as the ratio of response acceleration $\ddot{u}$ to maximum excitation acceleration $|\ddot{v}|_{max}$ and displacement signal is presented as the ratio of response displacement u to maximum excitation displacement $|v|_{max}$.

From Fig. 14 (a)-(c), response amplitude of GAS isolator increases with the increase of excitation acceleration. The acceleration ratio of the GAS isolator is less than 0.1, which demonstrates that GAS isolator shows good shock acceleration isolation performance under the given excitation level. Meantime, absolute displacement response is less than half of maximum excitation displacement. However, maximum relative displacement is larger than excitation displacement. As excitation level increases, natural period of residual vibration decreases, which demonstrates that effective dynamic stiffness of GAS isolator increases with the increase of excitation acceleration.

In Fig. 14(d)-(f), when load mass is smaller than 20.9 kg, shock acceleration response sharply decreases as load mass increases. However, when load mass is 23.4 kg, acceleration response amplitude is almost the same with that of 20.9 kg. From Fig. 14(e) and (f), it can be seen that natural period of residual vibration largely differs under different load masses, which agrees with the simulation results.

4.2.2. Shock transmissibility

Fig. 15 shows SAR, SAR and RDR under different excitation amplitudes and different payloads. The simulation results are in agreement with the experimental results, except that there are differences in the specific data points. From Fig. 15(a)-(c), it can be concluded that shock transmissibility of GAS isolator increases as the shock excitation amplitude increases. When

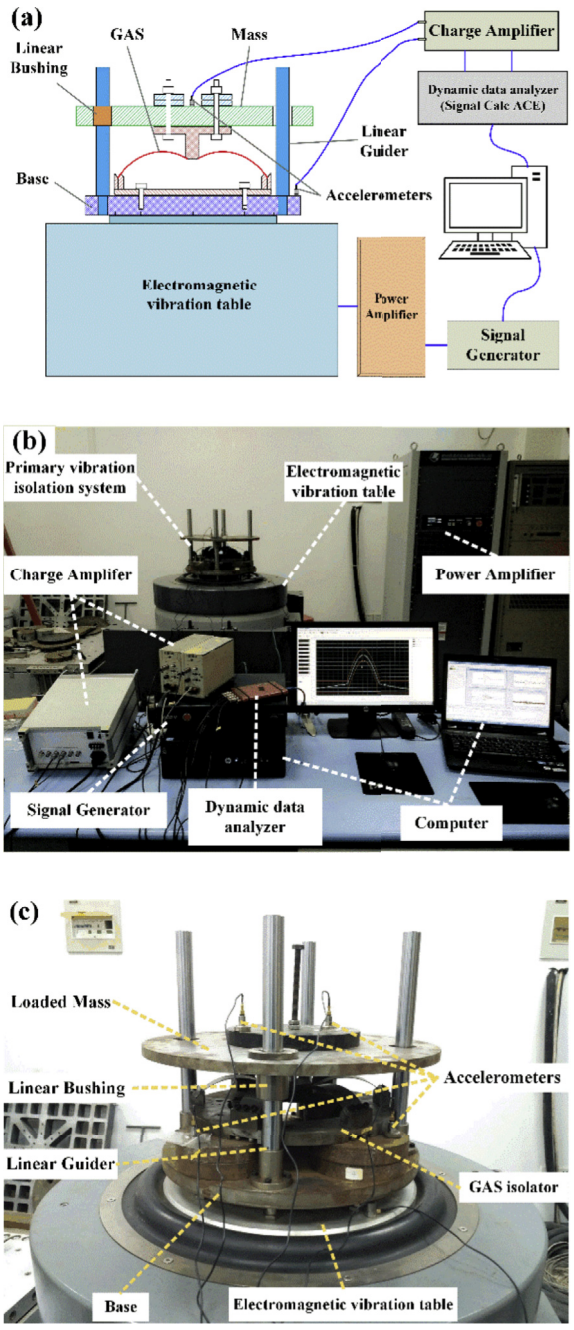

Fig. 12. Shock isolation experiment system. (a) Schematic diagram of the dynamic experiment system; (b) Photograph of the dynamic experiment system; (c) Photograph of the primary vibration isolation system.

severity parameter is large, shock pulse duration is short. So, shock input energy is small and system noise will largely influence the collection of response signals. The experiment results show the considerable difference with simulation results. Fig. 15(d)-(e) show that when load mass increases from 15.9 kg to 20.9 kg, SAR and SDR drop quickly. When load mass increased to 23.4 kg, SAR is the same as that of 20.9 kg and SDR increases just as like simulation results. RDR of GAS isolator first decreases and then increases with the increase of load mass. Maximum relative displacements are larger than maximum excitation displacement except for the situation of the duration of pulse 12 ms under load mass 18.4 kg.

According to the numerical and experimental results, the effects of excitation acceleration amplitude and payload on the shock isolation performance mainly vary with effective dynamic stiffness characteristics of the GAS isolator. With the increase of excitation amplitude, the effective dynamic stiffness of GAS isolator increases and shock transmissibility peak moves to the

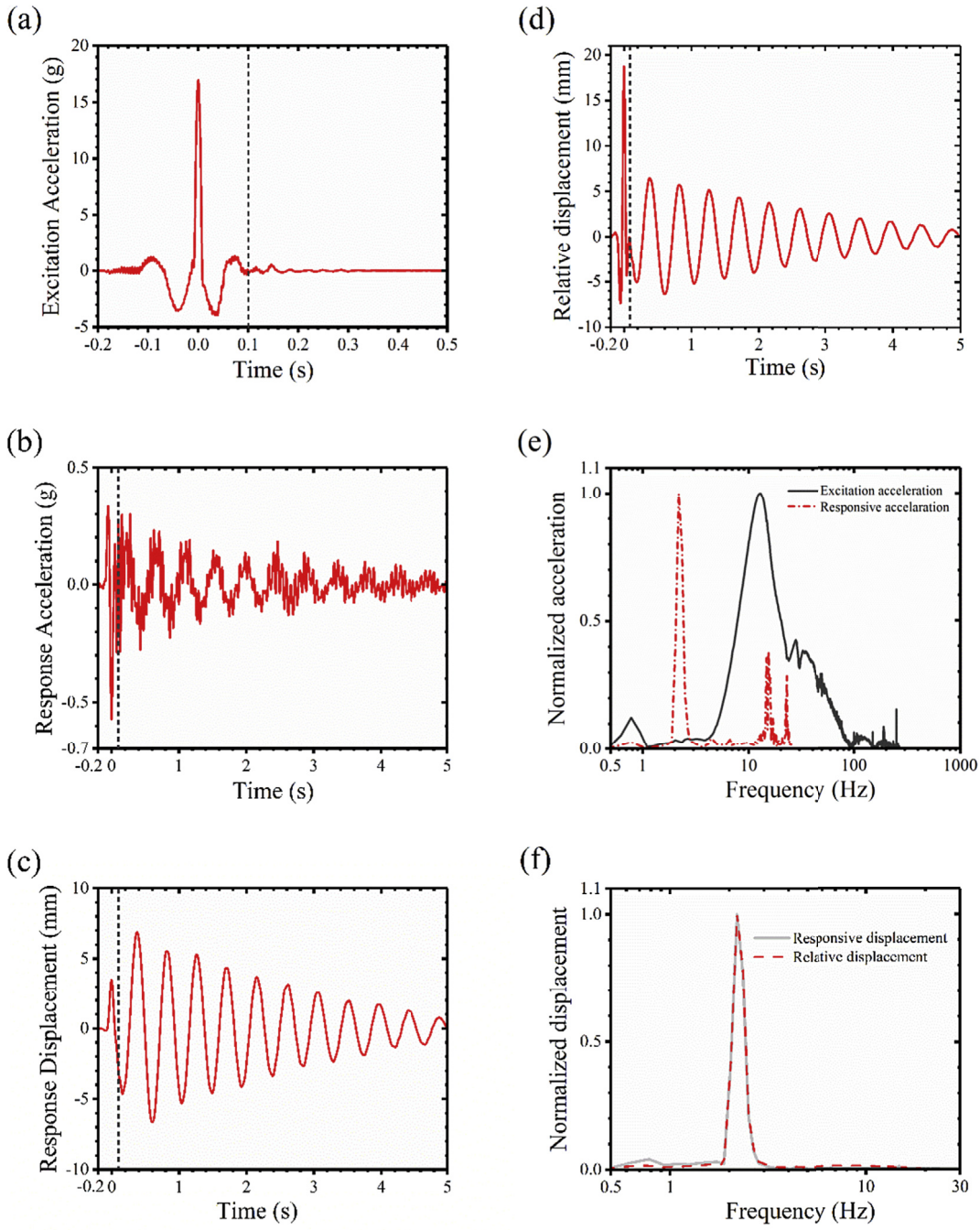

Fig. 13. Shock time domain response of GAS isolator with a payload of 20.9 kg under a shock excitation of 18 g and 16 ms. (a) Shock excitation acceleration. (b) Response acceleration of load mass. (c) Response displacement of load mass. (d) The relative displacement of the GAS isolator. (e) Frequency spectrums of excitation and responsive acceleration. (f) Frequency spectrums of response displacement of load mass and relative displacement.

position of larger severity parameter. As the payload increases, the effective dynamic stiffness of GAS isolator first decreases quickly and then increases slowly. Shock transmissibility of GAS isolator reduces fast at first and then increases as payload increases.

According to the experiment result of relative displacement of the GAS isolator, work ranges of force vs displacement curve for different payloads in shock experiment are calculated and shown in Fig. 16. In Fig. 16, the area, which surrounded by force vs displacement curve, a horizontal line through the static equilibrium point and two vertical lines through the final working

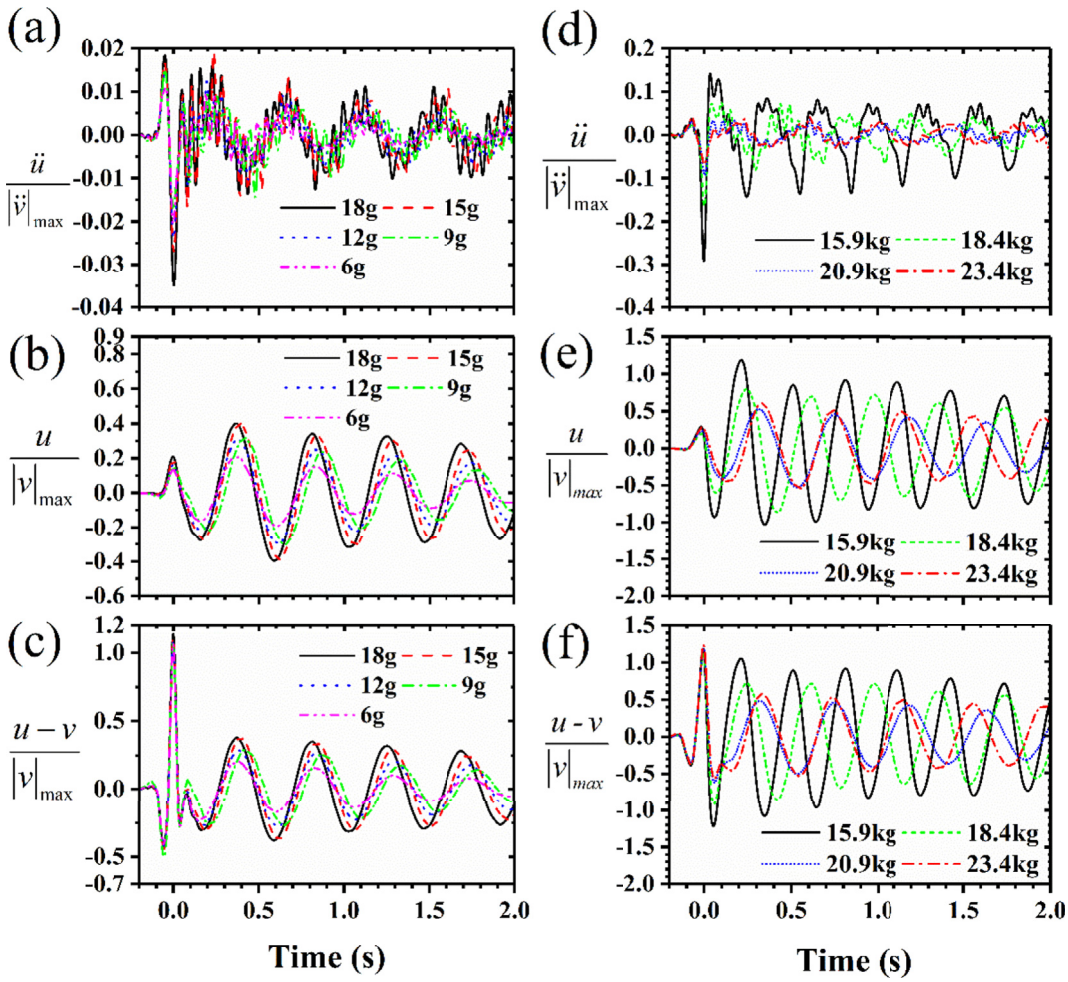

Fig. 14. Time domain response of GAS isolator. (a)–(c) are response acceleration, response displacement and relative displacement under different excitation levels with a shock pulse duration of 16 ms. (d)–(f) are response acceleration, response displacement and relative displacement under different payloads with the pulse duration of 22 ms and the excitation amplitude of 8 g.

point, denotes shock input energy approximately. When load mass is 20.9 kg, the maximum shock energy is represented by the area surrounded by $\widehat{OD}$, $\overline{OC}$ and $\overline{CD}$. For the equivalent linear isolator, according to the energy conservation law, the shock energy can be approximately represented by the area of ΔOAB. It is clear that relative displacement of equivalent linear isolator is smaller than that of GAS isolator. This can explain why RDR of GAS isolator is larger than that of equivalent linear isolator in shock isolation region. In amplification region, when relative displacement is large enough that nonlinear restoring force is larger than linear restoring force at maximum relative displacement point, the relative displacement of GAS isolator will be equal to or smaller than that of equivalent linear isolator.

5. Conclusion

In this paper, shock isolation performance of a GAS isolator subjected to double-sided compensation half-sine shock input is studied with numerical simulation. The shock isolation performance of GAS isolator under different excitation amplitudes and different payloads is experimentally investigated. Base on numerical and experimental results, some conclusion can be given as follows,

(1) The effective dynamic stiffness dominants shock isolation performance of GAS isolator. GAS isolator has an advantage on shock acceleration and displacement isolation in shock isolation region compared to the equivalent linear isolator. The smaller the geometric parameter is, the better the shock isolation performance will be. However, relative displacement ratio of the GAS isolator is larger than that of the equivalent linear isolator.

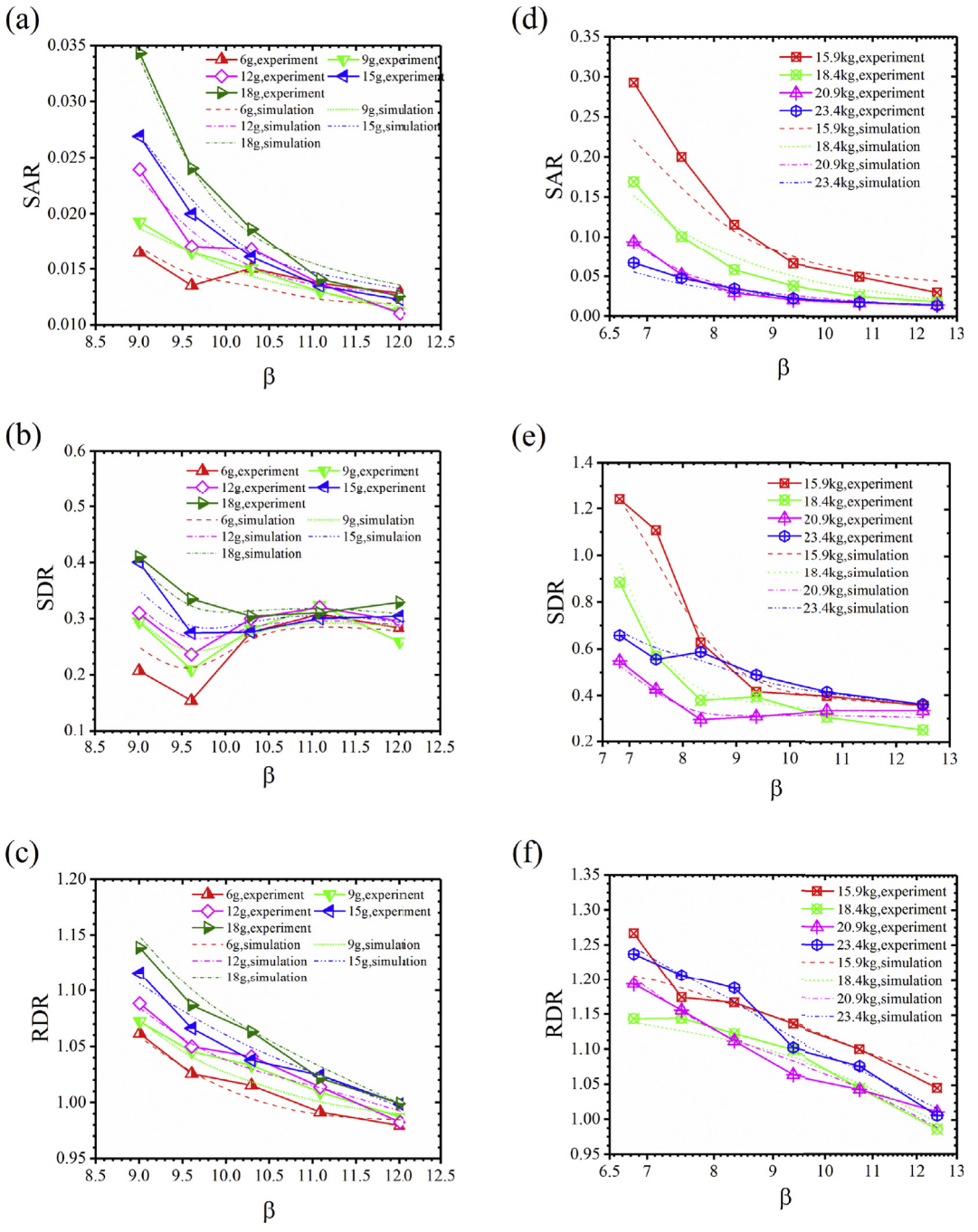

Fig. 15. Shock transmissibility of GAS isolator. (a)–(c) show SAR, SDR and RDR under different excitation amplitudes and (d)–(f) denote SAR, SDR, and RDR under different payloads.

(2) The increase of shock acceleration amplitude does not affect shock transmissibility in shock isolation region and in equivalent static loading region. Increasing shock acceleration amplitude, the range of shock amplification region of GAS isolator will be enlarged and the range of shock isolation region reduces.

(3) Change of payload will influence the shock isolation performance of GAS isolator. With increasing of the payload, shock transmissibility decreases first and then increase. The minimum shock transmissibility is obtained when GAS isolator working at the rated load.

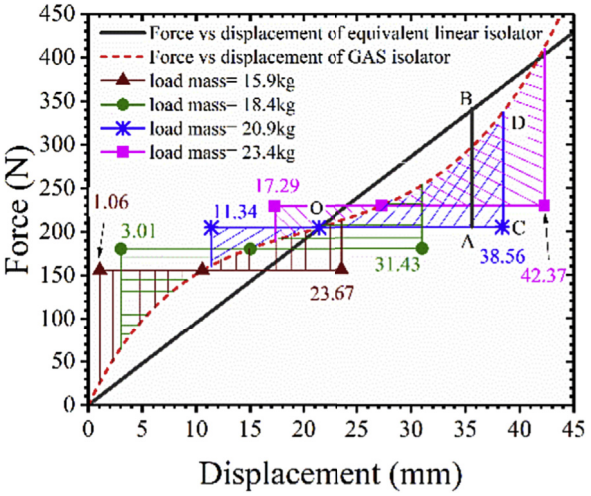

Fig. 16. Work ranges of force vs displacement curve for different payloads in shock experiment.

(4) Linear viscous damping shows a distinct effect in shock amplification region and shock isolation region. In shock amplification region, increasing damping ratio will reduce shock transmissibility curve peak. But too large damping ratio will increase shock acceleration and displacement transmissibility in shock isolation region.

Acknowledgment

Financial support from the Chinese Academy of Sciences (Grant No. XDB22040502) was gratefully acknowledged. This study was also supported by the Collaborative Innovation Center of Suzhou Nano Science and Technology.

References

[1] D. Francisco Ledezma-Ramirez, N. Ferguson, A. Salas Zamarripa, Mathematical modeling of a transient vibration control strategy using a switchable mass stiffness compound system, Shock Vib. 5 (2014) 1–10.
[2] J.C. Snowdon, Vibration and Shock in Damped Mechanical Systems, John Wiley & Sons, New York, 1968.
[3] R.S. Ayre, Engineering Vibrations, McGraw-Hill, New York, 2002.
[4] R.A. Ibrahim, Recent advances in nonlinear passive vibration isolators, J. Sound Vib. 314 (2008) 371–452.
[5] D.L. Platus, Negative stiffness-mechanism vibration isolation systems, Proc. Soc. Photo Opt. Ins. 1619 (1992) 44–54.
[6] H.J. Ahn, Performance limit of a passive vertical isolator using a negative stiffness mechanism, J. Mech. Sci. Technol. 22 (2008) 2357–2364.
[7] K.R. Kim, Y.H. You, H.J. Ahn, Optimal design of a QZS isolator using flexures for a wide range of payload, Int. J. Precis. Eng. Man. 14 (2013) 911–917.
[8] A. Carrella, T.P. Waters, M.J. Brennan, Static Analysis of a Quasi-zero-stiffness Vibration Isolator, 2006.
[9] T.D. Le, K.K. Ahn, Experimental investigation of a vibration isolation system using negative stiffness structure, Int. J. Mech. Sci. 70 (2013) 99–112.
[10] D.L. Xu, Y.Y. Zhang, J.X. Zhou, J.J. Lou, On the analytical and experimental assessment of the performance of a quasi-zero-stiffness isolator, J. Vib. Control 20 (2014) 2314–2325.
[11] C.C. Lan, S.A. Yang, Y.S. Wu, Design and experiment of a compact quasi-zero-stiffness isolator capable of a wide range of loads, J. Sound Vib. 333 (2014) 4843–4858.
[12] X.C. Huang, X.T. Liu, H.X. Hua, On the characteristics of an ultra-low frequency nonlinear isolator using sliding beam as negative stiffness, J. Mech. Sci. Technol. 28 (2014) 813–822.
[13] X.C. Huang, X.T. Liu, J.Y. Sun, Z.Y. Zhang, H.X. Hua, Vibration isolation characteristics of a nonlinear isolator using Euler buckled beam as negative stiffness corrector: a theoretical and experimental study, J. Sound Vib. 333 (2014) 1132–1148.
[14] J.X. Zhou, D.L. Xu, S. Bishop, A torsion quasi-zero stiffness vibration isolator, J. Sound Vib. 338 (2015) 121–133.
[15] A. Carrella, M.J. Brennan, T.P. Waters, Optimization of a quasi-zero-stiffness isolator, J. Mech. Sci. Technol. 21 (2007) 946–949.
[16] A. Carrella, M.J. Brennan, I. Kovacic, T.P. Waters, On the force transmissibility of a vibration isolator with quasi-zero-stiffness, J. Sound Vib. 322 (2009) 707–717.
[17] A. Carrella, M.J. Brennan, T.P. Waters, V. Lopes, Force and displacement transmissibility of a nonlinear isolator with high-static-low-dynamic-stiffness, Int. J. Mech. Sci. 55 (2012) 22–29.
[18] W.S.P. Robertson, B. Cazzolato, A. Zander, Horizontal stability of a Quasi-zero stiffness mechanism using inclined linear springs, Acoust. Aust. 42 (2014) 8–13.
[19] Z.F. Hao, Q.J. Cao, The isolation characteristics of an archetypal dynamical model with stable-quasi-zero-stiffness, J. Sound Vib. 340 (2015) 61–79.
[20] I. Kovacic, M.J. Brennan, The Duffing Equation: Nonlinear Oscillators and Their Behaviour, Wiley, 2011.
[21] A. Carrella, M.J. Brennan, T.P. Waters, K. Shin, On the design of a high-static-low-dynamic stiffness isolator using linear mechanical springs and magnets, J. Sound Vib. 315 (2008) 712–720.
[22] W.S. Robertson, M.R.F. Kidner, B.S. Cazzolato, A.C. Zander, Theoretical design parameters for a quasi-zero stiffness magnetic spring for vibration isolation, J. Sound Vib. 326 (2009) 88–103.
[23] D.L. Xu, Q.P. Yu, J.X. Zhou, S.R. Bishop, Theoretical and experimental analyses of a nonlinear magnetic vibration isolator with quasi-zero-stiffness characteristic, J. Sound Vib. 332 (2013) 3377–3389.
[24] Y.S. Zheng, X.N. Zhang, Y.J. Luo, B. Yan, C.C. Ma, Design and experiment of a high-static-low-dynamic stiffness isolator using a negative stiffness magnetic spring, J. Sound Vib. 360 (2016) 31–52.

[25] G.X. Dong, X.N. Zhang, S.L. Xie, B. Yan, Y.J. Luo, Simulated and experimental studies on a high-static-low-dynamic stiffness isolator using magnetic negative stiffness spring, Mech. Syst. Signal Process. 86 (2017) 188–203.
[26] A.D. Shaw, S.A. Neild, D.J. Wagg, P.M. Weaver, A. Carrella, A nonlinear spring mechanism incorporating a bistable composite plate for vibration isolation, J. Sound Vib. 332 (2013) 6265–6275.
[27] Z. Hu, G.T. Zheng, A combined dynamic analysis method for geometrically nonlinear vibration isolators with elastic rings, Mech. Syst. Signal Process 76–77 (2016) 634–648.
[28] L.N. Virgin, S.T. Santillan, R.H. Plaut, Vibration isolation using extreme geometric nonlinearity, J. Sound Vib. 315 (2008) 721–731.
[29] X.T. Sun, X.J. Jing, Analysis and design of a nonlinear stiffness and damping system with a scissor-like structure, Mech. Syst. Signal Process. 66–67 (2016) 723–742.
[30] Y. Araki, K. Kimura, T. Asai, T. Masui, T. Omori, R. Kainuma, Integrated mechanical and material design of quasi-zero-stiffness vibration isolator with superelastic Cu–Al–Mn shape memory alloy bars, J. Sound Vib. 358 (2015) 74–83.
[31] J.C. Snowdon, Transient response of nonlinear isolation mountings to pulselike displacements, J. Acoust. Soc. Am. 35 (1963) 389–396.
[32] A.E. Vakakis, Shock isolation through the use of nonlinear energy sinks, J. Vib. Control 9 (2003) 79–93.
[33] F. Georgiadis, A.F. Vakakis, D.M. McFarland, L. Bergman, Shock isolation through passive energy pumping caused by nonsmooth nonlinearities, Int. J. Bifurcat. Chaos 15 (2005) 1989–2001.
[34] D.F. Ledezma-Ramirez, N.S. Ferguson, M.J. Brennan, B. Tang, An experimental nonlinear low dynamic stiffness device for shock isolation, J. Sound Vib. 347 (2015) 1–13.
[35] B.A. Fulcher, D.W. Shahan, M.R. Haberman, C.C. Seepersad, P.S. Wilson, Analytical and experimental investigation of buckled beams as negative stiffness elements for passive vibration and shock isolation systems, J. Vib. Acoust. 136 (2014).
[36] X.C. Huang, Y. Chen, H.X. Hua, X.T. Liu, Z.Y. Zhang, Shock isolation performance of a nonlinear isolator using Euler buckled beam as negative stiffness corrector: theoretical and experimental study, J. Sound Vib. 345 (2015) 178–196.
[37] B. Tang, M.J. Brennan, On the shock performance of a nonlinear vibration isolator with high-static-low-dynamic-stiffness, Int. J. Mech. Sci. 81 (2014) 207–214.
[38] X.T. Liu, X.C. Huang, H.X. Hua, Performance of a zero stiffness isolator under shock excitations, J. Vib. Control 20 (2014) 2090–2099.
[39] G. Cella, V. Sannibale, R. DeSalvo, S. Marka, A. Takamori, Monolithic geometric anti-spring blades, Nucl. Instrum. Method A 540 (2005) 502–519.
[40] V. Sannibale, B. Abbott, Y. Aso, V. Boschi, D. Coyne, R. DeSalvo, S. Márka, D. Ottaway, A. Stochino, Recent results of a seismically isolated optical table prototype designed for advanced LIGO, J. Phys. Conf. Ser. 122 (2008) 012010.
[41] M.R. Blom, M.G. Beker, A. Bertolini, J.F.J. van den Brand, H.J. Bulten, E. Hennes, F.A. Mul, D.S. Rabeling, A. Schimmel, Seismic attenuation system for the external injection bench of the Advanced Virgo gravitational wave detector, Nucl. Instrum. Method A 718 (2013) 466–470.